



Mapping the tilt of the Milky Way bulge velocity ellipsoids with ARGOS and *Gaia* DR2

Iulia T. Simion¹★, Juntai Shen^{2,3}★, Sergey E. Koposov^{4,5,6}, Melissa Ness^{7,8}, Kenneth Freeman⁹,
Joss Bland-Hawthorn¹⁰ and Geraint F. Lewis¹⁰

¹Shanghai Astronomical Observatory, Chinese Academy of Sciences, 80 Nandan Road, Shanghai 200030, China

²Department of Astronomy, School of Physics and Astronomy, Shanghai Jiao Tong University, 800 Dongchuan Road, Shanghai 200240, China

³Key Laboratory for Particle Astrophysics and Cosmology (MOE)/Shanghai Key Laboratory for Particle Physics and Cosmology, Shanghai 200240, China

⁴Institute for Astronomy, University of Edinburgh, Royal Observatory, Blackford Hill, Edinburgh EH9 3HJ, UK

⁵Institute of Astronomy, University of Cambridge, Madingley Road, Cambridge CB3 0HA, UK

⁶McWilliams Center for Cosmology, Department of Physics, Carnegie Mellon University, 5000 Forbes Avenue, Pittsburgh, PA 15213, USA

⁷Department of Astronomy, Columbia University, Pupin Physics Laboratories, New York, NY 10027, USA

⁸Center for Computational Astrophysics, Flatiron Institute, 162 Fifth Avenue, New York, NY 10010, USA

⁹Research School of Astronomy and Astrophysics, Australian National University, Cotter Road, Weston, ACT 2611, Australia

¹⁰Sydney Institute for Astronomy, University of Sydney, School of Physics (A28), NSW 2006, Australia

Accepted 2021 January 7. Received 2021 January 7; in original form 2020 June 15

ABSTRACT

Until the recent advent of *Gaia* Data Release 2 (DR2) and deep multi-object spectroscopy, it has been difficult to obtain 6D phase space information for large numbers of stars beyond 4 kpc, in particular towards the Galactic Centre, where dust and crowding are significant. We combine line-of-sight velocities from the Abundances and Radial velocity Galactic Origins Survey (ARGOS) with proper motions from *Gaia* DR2 to obtain a sample of ~ 7000 red clump stars with 3D velocities. We perform a large-scale stellar kinematics study of the Milky Way bulge to characterize the bulge velocity ellipsoids in 20 fields. The tilt of the major-axis of the velocity ellipsoid in the radial-longitudinal velocity plane, or vertex deviation, is characteristic of non-axisymmetric systems and a significant tilt is a robust indicator of non-axisymmetry or bar presence. We compare the observations to the predicted kinematics of an N -body boxy-bulge model formed from dynamical instabilities. In the model, the l_v values are strongly correlated with the angle (α) between the bulge major-axis and the Sun-Galactic centre line of sight. We use a maximum likelihood method to obtain an independent measurement of α , from bulge stellar kinematics alone, performing a robust error analysis. The most likely value of α given our model is $\alpha = (29 \pm 3)^\circ$, with an additional systematic uncertainty due to comparison with one specific model. In Baade's window, the metal-rich stars display a larger vertex deviation ($l_v = -40^\circ$) than the metal-poor stars ($l_v = 10^\circ$) but we do not detect significant l_v –metallicity trends in the other fields.

Key words: Galaxy: bulge – Galaxy: kinematics and dynamics – Galaxy: structure – galaxies: individual: Milky Way.

1 INTRODUCTION

Being the nearest bulge to us and therefore the most accessible for deep observations, the Milky Way (MW) bulge has become the testbed for bulge formation theories in spiral galaxies. Over the past 20 yr, instrumentation advances have allowed us to custom-build photometric and spectroscopic surveys (see Babusiaux 2016 for a surveys list and references therein) to answer important questions about the bulge origin, structure, and evolution. Photometric surveys primarily focused on bright stars and were pivotal in revealing the bar morphology (Stanek et al. 1994; Robin et al. 2012; Wegg & Gerhard 2013; Simion et al. 2017). Spectroscopic surveys were crucial in proving the dynamical origin of the bar by providing line-of-sight velocities (Rich et al. 2007; Kunder et al. 2012; Ness et al. 2013b; Ness et al. 2016). Proper motions are difficult to measure at bulge

distances of 4–12 kpc as they are intrinsically small and therefore require great accuracy. Initially, only a small number of ~ 430 bulge stars possessed measurements of their transverse motions in a low extinction region named Baade's window (Spaenhauer, Jones & Whitford 1992). This number increased by three orders of magnitude with the NASA/ESA *Hubble Space Telescope* (HST; Kuijken & Rich 2002; Kozłowski et al. 2006; Clarkson et al. 2008; Soto, Kuijken & Rich 2012; Soto et al. 2014) and the Optical Gravitational Lensing Experiment II (OGLE II; Sumi et al. 2004; Rattenbury et al. 2007) which provided proper motions with accuracies of the order of 0.9–3.5 mas yr^{−1}, particularly in low extinction fields or along the bulge minor axis. The new generation surveys, the Vista Variables in the Via Lactea survey (VVV; Minniti et al. 2010; Smith et al. 2018), and more recently *Gaia* Data Release 2 (*Gaia* DR2; Gaia Collaboration 2016), have released proper motions for tens and hundreds of millions of bulge stars with sub-milliarcsecond accuracy.

In this work, we build a catalogue of bulge stars with full phase-space information to study the bulge velocity ellipsoids. In

* E-mail: isimion@shao.ac.cn (ITS); jtshen@sjtu.edu.cn (JS)

particular, we search for evidence of bulge triaxiality in our sample which contains proper motions from *Gaia* DR2 and radial velocities from the Abundances and Radial velocity Galactic Origins Survey (ARGOS; Freeman et al. 2013). Stellar kinematics studies were late to show any evidence of bulge triaxiality compared to star counts, measurements of the integrated light and kinematics of the atomic and molecular gas studies, which were all providing strong evidence that the bulge is triaxial and rapidly rotating already by the early ‘90s (de Zeeuw 1992). The main difficulty was obtaining accurate measurements at bulge distances, especially in the highly dust-obscured regions. The first study of bulge triaxiality from kinematics used a sample of 62 K giants (Zhao, Spergel & Rich 1994) with proper motions, radial velocities, and metallicities in Baade’s window at $(l, b) = (1^\circ, -4^\circ)$. The distributions of these stars projected on to three velocity planes (v_l-v_b , v_l-v_r , and v_r-v_b) were fitted by velocity ellipsoids with Gaussian profiles (Zhao et al. 1994). Although the velocity distribution in the v_l-v_r diagram was symmetric with respect to the v_r and v_l axes, the long axis of the velocity ellipsoid appeared tilted at an angle l_v with the longitudinal velocity v_l axis. The orientation of the axis of the velocity ellipsoid in the v_l-v_r plane, l_v or vertex deviation, is a measure of the correlation between the radial and longitudinal velocities and is affected by the bulge non-axisymmetry. In an axisymmetric bulge, l_v should be consistent with $l_v \sim 0^\circ$ along the minor axis ($l \sim 0^\circ$). However, the metal-rich stars in Baade’s window have $l_v \sim 40^\circ$ (Zhao et al. 1994; Babusiaux et al. 2010; Soto et al. 2012); this was the ‘first clear evidence for vertex deviation, a ‘smoking gun’ of bulge triaxiality’ (Zhao et al. 1994). On the other hand, the v_l-v_b and v_r-v_b diagrams did not display significant l_v . Soto, Rich & Kuijken (2007) confirmed this result with an expanded data set of ~ 300 stars, in the same region. The addition of spectroscopic measurements made it possible to study the variation of the vertex deviation with metallicity (Babusiaux et al. 2010; Hill et al. 2011; Ness et al. 2013a), suggesting that only the more metal-rich stars display a tilted velocity ellipsoid distribution. For a review on the correlations between kinematics and metallicity prior to *Gaia* DR2, see Babusiaux 2016. Simulations have shown that the metal-poor and metal-rich components have different spatial distributions (Debattista et al. 2017) which could explain the difference in the vertex deviation trends with metallicity. Perhaps the most complete 3D sample to date was provided by Soto et al. (2012), who compiled a sample of ~ 3200 stars observed by *HST* and VLT, in 6 bulge fields. They used *HST* proper motions and VLT/VIMOS Integral Field Unit (IFU) radial velocities with $\sim 1 \text{ mas yr}^{-1}$ and 50 km s^{-1} accuracies, respectively.

The sample we use in this work contains ~ 7000 likely red clump (RC) bulge stars with $<0.5 \text{ mas yr}^{-1}$ proper motions and 1 km s^{-1} radial velocity accuracies, respectively, distributed in 20 fields across the bulge, following the ARGOS footprint. RC stars are excellent standard candles, with a luminosity weakly dependent on age and metallicity, providing 5–10 per cent distance uncertainties (Stanek et al. 1997; Girardi 2016; Hawkins et al. 2017). We could thus obtain the full phase-space information for our sample. The ARGOS fields of view are situated at latitudes beyond 4° from the plane, avoiding the high extinction regions close to the Galactic plane, spiral arms and the long thin bar (e.g. Wegg, Gerhard & Portail 2015; Wegg et al. 2019). Our catalogue is suitable for studying the kinematics of the boxy/peanut bulge, successfully traced by star count studies using RC stars. Studies with RC stars have consistently reported that the bulge is triaxial with the major axis at an angle $\alpha \approx 20\text{--}30^\circ$ with respect to the Sun-Galactic Centre line (Stanek et al. 1997; Cao et al. 2013; Wegg & Gerhard 2013; Simion et al. 2017). Asymmetries in

the star counts (Stanek et al. 1997) show that the near end of the bar is situated at positive longitudes.

This work investigates the relationship between the bulge velocity ellipsoid evidenced by our data sample and the bulge non-axisymmetric density distribution induced by the viewing angle α , with the help of a numerical model. Numerical models of a boxy bar/bulge where the angle α can be easily varied, are helpful to study the relationship between the two and interpret the observations.

Earlier bulge models (Zhao et al. 1994; Häfner et al. 2000) were built and scaled to reproduce the morphological, chemical, and kinematic properties of the MW, providing precious insight into the chemodynamical history of the bulge. It is generally agreed that the MW hosts a boxy bulge (Kormendy & Kennicutt 2004), which forms from a bar instability in the disc and is subsequently thickened probably by the buckling instability (Raha et al. 1991; Debattista et al. 2005; Martinez-Valpuesta, Shlosman & Heller 2006; Shen et al. 2010). Other bar thickening mechanisms involving resonant heating were discussed by e.g. Combes et al. (1990), Quillen et al. (2014), and Sellwood & Gerhard (2020). The evolution of these bulges is affected by the exchange in angular momentum with the disc and dark halo, and the in-plane and vertical stellar motions (Debattista et al. 2017; Fragkoudi et al. 2017; Di Matteo et al. 2019). There is consensus between radial velocity (Howard et al. 2009) and proper motion (Clarke et al. 2019; Sanders et al. 2019b) surveys that the bulge rotates cylindrically with the rotational velocity profile almost independent of height, a behaviour that is well matched by fully evolutionary N -body models of boxy/peanut bulges formed through internal dynamical instabilities in the disc (Shen et al. 2010; Qin et al. 2015). Such models also naturally explain the existence of an X-shaped structure visible at intermediate latitudes in the MW bulge (McWilliam & Zoccali 2010; Nataf et al. 2010, 2015; Saito et al. 2011; Li & Shen 2012; Nataf, Cassisi & Athanassoula 2014; Ness & Lang 2016; Shen & Li 2016). The 3D kinematics through the X-shape was studied by Vázquez et al. (2013). While the MW has an obvious boxy bulge, the presence of a ‘classical’ bulge has not been completely excluded (Shen et al. 2010; Saha & Gerhard 2012). ‘Classical’ bulges form differently from boxy bulges, either through hierarchical merging (Bender, Burstein & Faber 1992) or monolithic collapse (Eggen, Lynden-Bell & Sandage 1962), in a similar fashion to mini-elliptical galaxies.

While our work falls in line with the studies of Zhao et al. (1994) and Soto et al. (2012), there are several studies which use models to explain the observed links between kinematics and metallicity, or morphology and metallicity. Athanassoula, Rodionov & Prantzos (2017) found good qualitative agreement between the observed radial velocity dispersion variations in the bulge as a function of metallicity (Ness et al. 2013b; Babusiaux 2016; Zasowski et al. 2016) and the output of a numerical simulation which included gas/star formation and a major merger event (Athanassoula et al. 2016). Debattista et al. (2019) used a cosmological simulation from the FIRE¹ project to study the vertex deviation as a function of age and metallicity in Baade’s window. In agreement with the observations, they find that the high-metallicity population has a large vertex deviation ($l_v \sim 40^\circ$) while it is negligible for metal poor stars. The variation of l_v with age has not yet been studied in observations, but Debattista et al. (2019) find that the younger stars display a higher vertex deviation than older ones (their fig. 10). The same l_v trends with age and metallicity can be observed even if the accreted stars are not included, proving that they are not necessarily caused by an accreted population.

¹<https://fire.northwestern.edu/>.

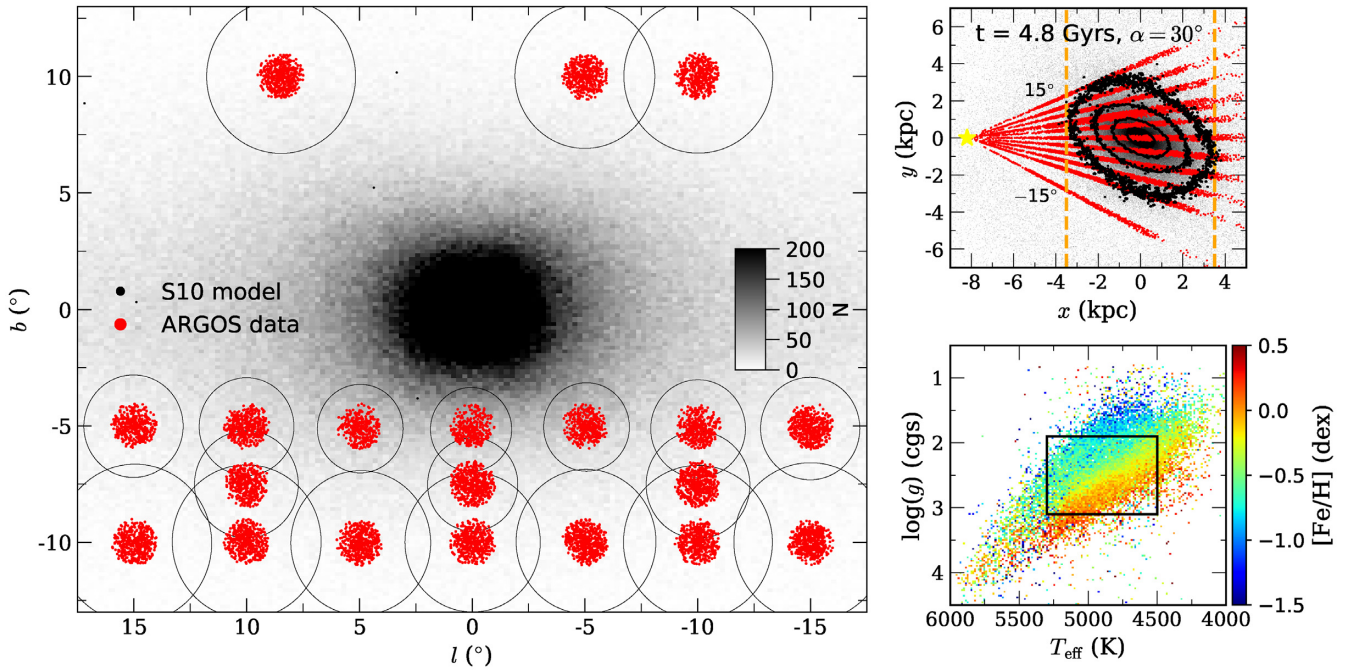


Figure 1. *Left-hand panel:* The ARGOS survey (red) and the S10 model (grey), in Galactic coordinates. The number of particles in the model decreases dramatically with distance from the Galactic plane: to select at least 2000 simulation particles around each ARGOS pointing, we vary the radius of the simulation fields of view, each centred on a survey pointing. *Top right panel:* Projection on to the x - y plane of the ARGOS data set and the simulation for a bar viewing angle of 30° . In this configuration, the Sun is located at $x_\odot = -8.3$ kpc, $y_\odot = 0$ kpc and the positive longitudes are in the direction of positive y . The near end of the bar is at $x < 0$ kpc and $l > 0^\circ$. To minimize contamination from foreground stars, we only select stars within $|x| < 3.5$ from the Galactic Centre (vertical orange lines). *Bottom right panel:* H-R diagram of the ARGOS stars with *Gaia* DR2 proper motions. Stars within the black box are likely RC stars. To build a clean sample of bulge RC stars with 6D phase-space information, we also perform proper motion error cuts in addition to the x distance, $\log(g)$, and T_{eff} selection.

In this work we aim to perform a quantitative comparison between observations and a self-consistent N -body simulation of bar formation, focusing on the links between bulge kinematics and bulge morphology. In particular, we study the relationship between the tilt of the velocity ellipsoid l_p and the bar viewing angle α .

In Section 2, we describe the data selection and the N -body boxy bulge model (Shen et al. 2010, thereafter the S10 model). In Section 3, we map the bulge velocity ellipsoids as seen in the data and the simulations while in Section 4 we outline the fitting method and present the results. In Section 5, we add a new dimension to our 6D sample, the metallicity, and in Section 6 we present the conclusions.

2 DATA AND THE N -BODY BOXY BULGE MODEL

2.1 Data

The data originate from two surveys, ARGOS and *Gaia* DR2.

2.1.1 ARGOS

ARGOS is a spectroscopic survey of 28 000 predominantly giant stars in 28 fields (Freeman et al. 2013; Ness et al. 2013b), selected for follow-up from the Two Micron All Sky Survey (2MASS; Skrutskie et al. 2006), in the magnitude range $K = 11.5$ –14 mag. The observations were taken with the AAOmega multi-fiber spectrograph on the Anglo Australian Spectrograph at the Siding Spring Observatory, which can observe up to 340 stars simultaneously. We are interested in studying the bulge kinematics therefore we focus only on the 20

fields (marked in red in Fig. 1, left-hand panel) that are closest to the main bulge population. The fields have a diameter of $\sim 2^\circ$ and in each field around 1000 stars were randomly observed.

The radial velocity v_r , effective temperature T_{eff} , surface gravity $\log(g)$, metallicity $[\text{Fe}/\text{H}]$, and alpha element abundance $[\alpha/\text{Fe}]$ were determined for each star using the ARGOS stellar pipelines (Ness et al. 2012). Radial velocities were computed via cross-correlation with synthetic spectra and, at the ARGOS typical resolution of $R = 11\,000$ and $\text{S/N} \sim 50$ –80, the velocity errors are smaller than 1.2 km s^{-1} (Freeman et al. 2013). In the following sections, we assume a constant value of $\delta_{v_r} = 1 \text{ km s}^{-1}$.

The distances were computed for the whole ARGOS sample via isochrone fitting (Ness et al. 2013a), but we choose to work only with a subsample of RC stars as they are great distance indicators and possess smaller distance uncertainties. The RC stars are selected based on their temperature and surface gravity, $4500 < T_{\text{eff}}/\text{K} < 5300$, $1.9 < \log(g) < 3.1$, as marked by the black lines in the ARGOS Hertzsprung–Russell (H–R) diagram (bottom right panel of Fig. 1; see also figs 2 and 3 from Ness et al. 2013a). Despite these cuts, the contamination from the background population of red giant branch (RGB) stars could be up to 30 per cent (Freeman et al. 2013). It is difficult to separate the RC from the RGB but in this selection box, centred on the RC, they should have similar intrinsic brightness (see a model intrinsic luminosity curve for bulge giants in Simion et al. 2017, fig. 3). For the stars that are not RC, the M_K values were derived using isochrone fitting (Freeman et al. 2013). Reassuringly, we find a very close agreement between the distances provided by ARGOS and the distances computed directly from the extinction corrected photometry using the absolute magnitude value of the

RC, $M_K \sim -1.61$ mag (Alves 2000; Hawkins et al. 2017) for our selected sample. The largest source of uncertainty is the spread of the RC absolute magnitude, $\delta_{M_K} \sim 0.22$ mag (Alves 2000; Ness et al. 2013a), which gives uncertainties $\lesssim 1.5$ kpc at the bulge distances. The errors due to 2MASS photometry and interstellar reddening are small at the ARGOS survey latitudes of $|b| > 4.5^\circ$.

In the top right panel of Fig. 1, we show the projection of the ARGOS RC stars on to the x - y plane, where the Sun is placed at $(x_\odot, y_\odot, z_\odot) = (-8.3, 0, 0)$ kpc (Gillessen et al. 2017). While The GRAVITY Collaboration (2019) found $x_\odot = 8178$ pc, we do not expect the small difference to impact our study, as the RC distances and transverse velocities dominate the uncertainties. We adopt a left-handed Galactic Cartesian system with the x -axis positive in the direction of the Galactic Center, y -axis oriented along the Galactic rotation and the z -axis directed towards the north Galactic pole. In the following analysis, we only select stars within $|x| < 3.5$ kpc (orange lines in top right panel of Fig. 1) from the Galactic Centre (GC) $(x, y) = (0, 0)$ kpc in order to minimize contamination from disc and foreground stars.

2.1.2 GAIA DR2

Gaia DR2 provides accurate proper motions measurements for the majority of ARGOS stars: from the initial ARGOS sample, we discard targets which do not have a *Gaia* DR2 counterpart or have large proper motions uncertainties $\sigma_{\mu_{RA}}, \sigma_{\mu_{Dec}} > 0.2$ mas yr $^{-1}$. The cross-matching between ARGOS and the 2MASS – *Gaia* DR2 value added catalogue was done within a 1 arcsec radius but, after applying the proper motions error selection, all matches were within 0.3 arcsec with a mean angular distance of 0.05 arcsec. We have also checked that the K magnitudes in the ARGOS and 2MASS – *Gaia* DR2 catalogues were matching. Finally, our sample of bulge RC stars with complete 6D phase-space information amounts to ~ 7000 stars, or around 400 stars per pointing.

In Fig. 2, we show the median of the 3 velocity components in each ARGOS field from Fig. 1: the line-of-sight velocity v_r (top panel), the longitudinal velocity v_l (middle panel), and latitudinal velocity v_b (bottom panel). Only stars in front of the GC ($-3.5 < x/\text{kpc} < 0$) are shown because the ARGOS sample is more complete at nearby heliocentric distances than behind the GC. The velocities were corrected for the Solar reflex motion assuming the default *astropy* values for the Sun's peculiar motion, $(U, V, W) = (11.1, 12.24, 7.25)$ km s $^{-1}$ (Schönrich, Binney & Dehnen 2010) and for the circular velocity at solar radius, 220 km s $^{-1}$. From these maps, it is immediately clear that the stars do not have random motions: the stars at positive/negative longitudes have positive/negative radial velocities, respectively, resulting from a perspective effect of the approaching right side versus retreating left side of the bar (see also Ness et al. 2013b). The v_l velocities are all positive, as expected for stars in front of the bar (Qin et al. 2015, fig. 4). The v_b velocities are small across the bulge, within $|v_b| < 50$ km s $^{-1}$, compared to the values of v_r and v_l .

Beyond $|l| > 10^\circ$, the central boxy-peanut bulge of the MW transitions to a longer, flatter bar which extends out to $l \sim 25^\circ$ (e.g. Wegg et al. 2015, fig. 9); however, being limited by the survey to fields beyond $|b| > 4.5^\circ$, the long (thin) bar is not visible in our $l \sim \pm 10^\circ, \pm 15^\circ$ fields. At $l \sim 20^\circ$, the outermost longitude of ARGOS which is not considered in this work, the long bar lies at a distance of ≈ 5.2 kpc from the Sun and a height above the plane of 180 pc, still well below the ARGOS visibility threshold of ~ 400 pc at this distance. Therefore, we can safely assume that the long bar does not affect the kinematics observed in the fields considered in this work, and we do not discuss it in the next sections.

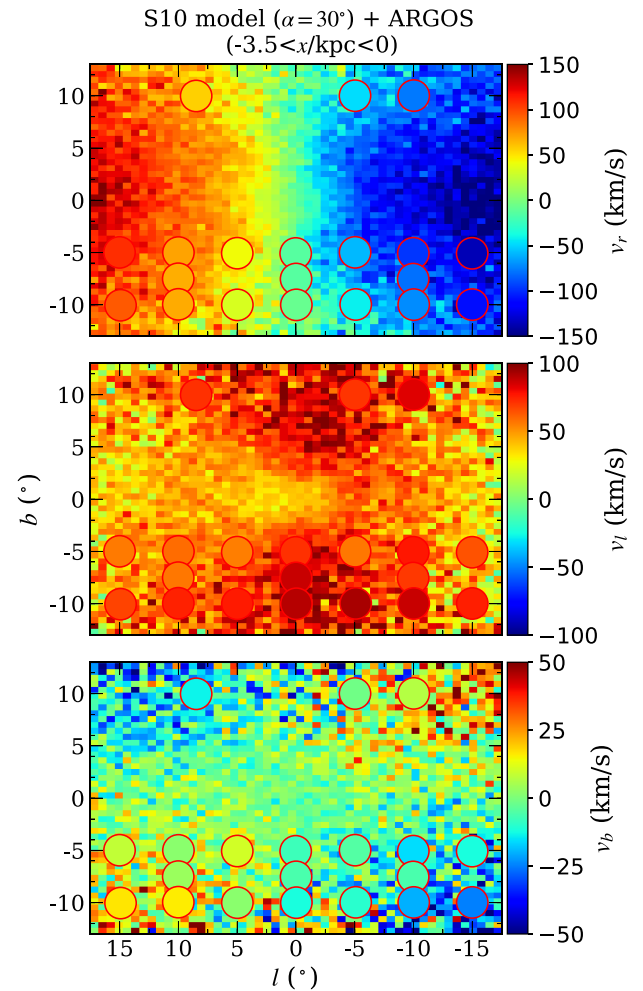


Figure 2. *Top panel:* Radial velocity map of the S10 model and, overlaid, the median radial velocity in each ARGOS pointing, in Galactic Coordinates. Only stars with $-3.5 < x/\text{kpc} < 0$ (in front of the GC) are shown, to facilitate the comparison between the simulation and the data, which are less complete behind the GC. *Middle panel:* same as above, but for v_l . Stars in front of the GC, due to the bar's rotation, move from left (negative longitudes) to right (positive longitudes) causing v_l to be positive. In addition, there is little variation with latitude because the bulge rotates approximately cylindrically. *Bottom panel:* Same as above, but for v_b . The vertical motion is small (notice the colour-scale change) with $|v_b| \lesssim 50$ km s $^{-1}$.

2.2 Simulations

We use the S10 model, an N -body simulation with 1 million disc particles rotating in a rigid dark matter potential. In this model, a bar is formed in the early stages of evolution which buckles to produce a boxy peanut shaped bulge. The S10 model is successful at reproducing and explaining some of the observed morphological bar properties such as the double red clump, X-shape, and kinematics (Li & Shen 2012; Molloy et al. 2015a, b; Nataf et al. 2015; Qin et al. 2015). The simulation does not include gas and star formation therefore is expected to characterize the kinematics of the older bulge stellar population. As newly formed stars reside closer to the Galactic Plane (Debattista et al. 2015) and ARGOS is limited to $|b| > 4.5^\circ$, we are not concerned with the highly star-forming disc regions.

Strong variations in the bar pattern speed Ω_p (of the order of ± 10 km s $^{-1}$ kpc $^{-1}$) are expected to have an effect on the bulge

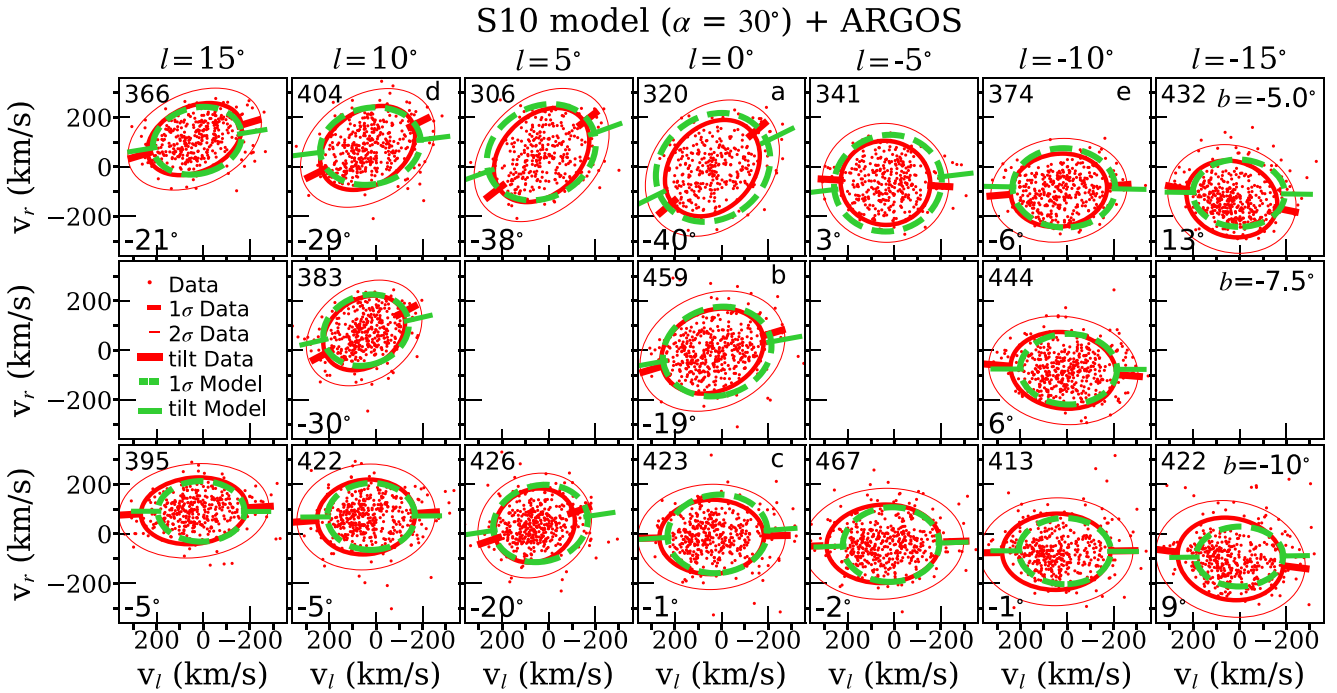


Figure 3. Velocity ellipsoids for the ARGOS survey (each panel corresponds to a pointing in Fig. 1). The 68 and 95 per cent contours of the ARGOS velocity distributions are shown in red, and the 68 per cent contour of the distance-resampled S10 model (see Fig. 4) with a viewing angle of 30° , in green. The tilt of the ellipsoids l_v is indicated by the red/green lines which extend between the 68 and 95 per cent contours of the data/simulation velocity ellipsoids. The number of ARGOS RC bulge stars (red points) in each panel is given in the top-left corner and the corresponding l_v value in the bottom-left corner. The l_v values of the distance-resampled S10 model and the data are also shown in Fig. 6.

mean radial velocities and velocity dispersions (see Portail et al. 2017, fig. 10). However, the bar pattern speed in the S10 model, $\Omega_P \sim 40 \text{ km s}^{-1} \text{ kpc}^{-1}$ (Shen 2014), matches closely the MW value measured from kinematics: Portail et al. (2017) computed $\Omega_P = 39 \pm 3.5 \text{ km s}^{-1} \text{ kpc}^{-1}$ using ARGOS data and, more recently, Sanders, Smith & Evans (2019a) found $\Omega_P = 41 \pm 3 \text{ km s}^{-1} \text{ kpc}^{-1}$ using proper motions from *Gaia* DR2 and VVV. Because the bar pattern speed Ω_P of the model closely matches the observations, we do not expect it to be the cause of significant kinematic differences between the data and the model.

A first qualitative comparison between our data and the S10 model kinematics is shown in Fig. 2, within the $-3.5 < x/\text{kpc} < 0$ distance range (in front of the GC). For the S10 model, we assume a bar viewing angle of $\alpha = 30^\circ$. The three panels of the figure are maps of the median velocity values of the three velocity components in the S10 model. The median velocities in each ARGOS field are shown with colour-coded circles (see Section 2.1). The S10 maps look similar for different bar viewing angles α within the same distance range. If we considered the region with $0 < x/\text{kpc} < 3.5$ (behind the GC), only the v_l map would change significantly as stars at these distances have $v_l < 0 \text{ km s}^{-1}$. Overall, the velocity trends observed in the data and the S10 model are consistent. In the next sections, we perform a quantitative comparison between the two.

3 BULGE VELOCITY ELLIPSOIDS

3.1 Data

The ARGOS velocity distributions in the radial-longitudinal velocity plane are shown in Fig. 3, where each subpanel corresponds to a survey pointing, excluding the three fields with $b > 0^\circ$. The near-

end of the bar is situated at positive longitudes, in the left-hand side of the figure, while the far-end is situated at negative longitudes in the right-hand side. For any line of sight, we model the velocity distributions along the longitudinal (l), radial (r), and latitudinal (b) velocity directions with a single-component 3D Gaussian. We assume that the distributions in each pointing are Gaussian although we might expect deviations from Gaussianity due to incomplete sampling and large measurement uncertainties for the stars on the far side of the bar. To compute the model likelihood we use the Extreme Deconvolution (ED; Bovy, Hogg & Roweis 2011) method implemented in the astroML (Vanderplas et al. 2012) package. In Fig. 3, we show the contours containing 68 per cent (thick red line) and 95 per cent (thin red line) of the ARGOS velocity distributions fitted in each individual field. The number of RC stars that satisfy all the selection criteria outlined in Section 2 and that are used to fit the velocity ellipsoid is given in the upper left corner of each subpanel.

The ED method requires that the uncertainty of each velocity component $\delta_{V_i} = \{\delta_{v_l}, \delta_{v_b}, \delta_{v_r}\}_i$ is provided. For each star we have the 6D phase-space information (see Section 2) provided by the *Gaia* – ARGOS cross-match $\{\alpha, \delta, D, \mu_{\alpha^*}, \mu_\delta, v_r\}_i$. The uncertainties δ_{V_i} are computed via Monte Carlo re-sampling where the diagonal terms of the covariance matrix are the *Gaia* DR2 errors on the right ascension σ_{α^*} , declination σ_δ , and proper motions $\sigma_{\mu_{\alpha^*}}, \sigma_{\mu_\delta}$ and the ARGOS heliocentric distance uncertainties σ_D and radial velocity error of 1 km s^{-1} . The *Gaia* cross-terms between the coordinates $\rho(\alpha, \delta)$ and proper motion components $\rho(\mu_{\alpha^*}, \mu_\delta)$, including $\rho(\alpha, \mu_\delta)$ and $\rho(\delta, \mu_{\alpha^*})$, are also taken into account. We use the standard deviation of 1000 evaluations of $V_i = \{v_l, v_b, v_r\}$ as an estimate of the star's velocity uncertainty δ_{V_i} . Because the uncertainties on the v_l and v_b components are dominated by the distance errors, our most uncertain measurement, they can reach $\sigma_{v_l}, \sigma_{v_b} \sim 30\text{--}40 \text{ km s}^{-1}$.

3.2 Simulations

For each particle in the **S10** model, the 6D phase space $\{x, y, z, v_x, v_y, v_z\}_i$ is provided in the Galactocentric frame. The transformations to the Galactic frame were performed using `galpy`. The advantage of using a simulation is that we can adopt any angle between the Sun-GC line and the bar major axis, α , by rotating the reference frame. The simulation particles are selected from circular fields of varying radius, centred on the ARGOS fields. As the density of particles drastically diminishes with distance from the Galactic Centre, we increase the radius of the simulation fields with increasing longitude and latitude (black circles in Fig. 1), so that each field contains approximately 2000 particles within $|x| < 3.5$ kpc. From Fig. 1, it is clear that the simulation fields at $b = \pm 10^\circ$ are significantly bigger than the corresponding ARGOS fields but we do not expect a small difference in field size to have a major effect on the kinematics of stars at these latitudes as they are situated on the outskirts of the main bulge population (see the number density map in grey, in the left-hand panel of Fig. 1).

In Fig. 3, we show the 68 per cent contour (green dotted line) of the **S10** model velocity distributions within each simulation field, for $\alpha = 30^\circ$. The model closely matches the data 68 per cent contour (red line) in most fields. The distance distribution of the simulation particles was resampled according to the distribution of the ARGOS distances, with a process detailed in Fig. 4. In the left column of the figure we show the model for two α values and in right column we show the distance distribution of the simulation particles before resampling (black histogram) in 5 fields: 3 along the minor axis (labelled a, b, c), one on the near end of the bar (d) and one on the far side of the bar (e). While the **S10** model particles are concentrated around the GC as expected from star count models (e.g. Simion et al. 2017), the distribution of the ARGOS distances (red histogram) is skewed, with the majority of stars located in front of the GC, likely due to a mismatch between the **S10** model density and the MW bulge density distribution, incomplete survey sampling, extinction, and magnitude limits. The distance to the stars is important as the stellar kinematics varies within the bar: for example, the 2D velocity distribution of ARGOS stars (red points) in Figs 3 and 4 shows there is a higher concentration of stars for $v_l > 0$ km s $^{-1}$ values than for $v_l < 0$ km s $^{-1}$, which is to be expected if the majority of stars is in front of the bar (Qin et al. 2015). Therefore, to build a model that best describes the data, we resample the particles in the simulation to follow the same distance distribution as the ARGOS RC stars in each field.

Before resampling, to mimic the observational procedure, we randomly perturb the heliocentric distances D in the simulation, which are unaffected by errors, by the typical uncertainties expected for RC stars of $\delta_{M_K} \sim 0.22$ mag assuming a Gaussian error distribution with a standard deviation of $\sigma_D \approx \delta_{M_K} \times 0.2 \times D \times \ln(10)$. From the perturbed sample we draw 25000 random particles, allowing for duplicates, according to the probability distribution of the ARGOS distances (red histogram in Fig. 4), modelled with a kernel density estimation (KDE) in each individual pointing. The probability density distribution of the resampled **S10** model distances is shown with a green histogram in Fig. 4 and it closely matches the data, red histogram, by construction.

We also add realistic velocity errors to the simulation particles. In each field of view, we assign the median ARGOS velocity uncertainty of stars in that field, to each **S10** model particle. The 3D velocity distribution of these particles is then fitted with a multivariate Gaussian, for a specified viewing angle α , in each individual pointing. In the right column of Fig. 4 we show the 68 per cent contours of two models, one with the near end of the bar at positive longitudes

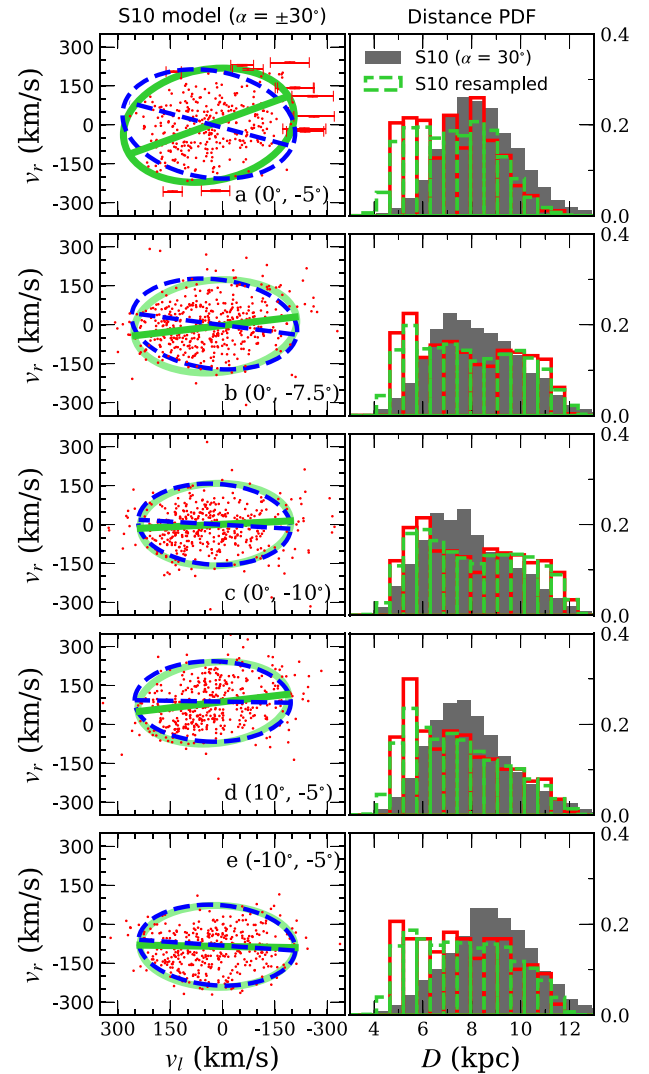


Figure 4. *Left-hand panels:* To find the most likely bar viewing angle from the ARGOS velocity distribution, we compute the probability of the data (red points) to belong to a model velocity ellipsoid fitted on the distance-resampled **S10** model. We show the model for 2 bar angles, $\alpha = -30^\circ$ (blue) and $\alpha = 30^\circ$ (same as in Fig. 3, green). For one field, we have added the uncertainties on the v_l component for stars outside the 68 per cent contour. The errors vary between 15 and 50 km s $^{-1}$, with larger values for the stars behind the bar, which have $v_l < 0$ km s $^{-1}$. In the fields labelled c, d, and e, the vertex deviation is $l_v \approx 0^\circ$ for both models, indicating that these fields are not good predictors of the bar viewing angle. On the other hand, the model velocity ellipsoids and the tilt of their major axis, are different in the a, b fields, for the two angles. *Right-hand panels:* The distance distribution of the simulation particles is centred on the GC (black histogram) but the data tend to have more stars in front of the bar (red histogram) due to the survey sampling. The models shown in the left column correspond to a resampled distance probability distribution (green histogram), which matches the data distance distribution.

$l > 0^\circ$ and $\alpha = 30^\circ$ (green) and one with the near end of the bar at negative longitudes $l < 0^\circ$ and $\alpha = -30^\circ$ (dotted blue line). The model in Fig. 3 (green line, $\alpha = 30^\circ$) is identical to the one in Fig. 4 and is also computed using the distance-resampled **S10** model.

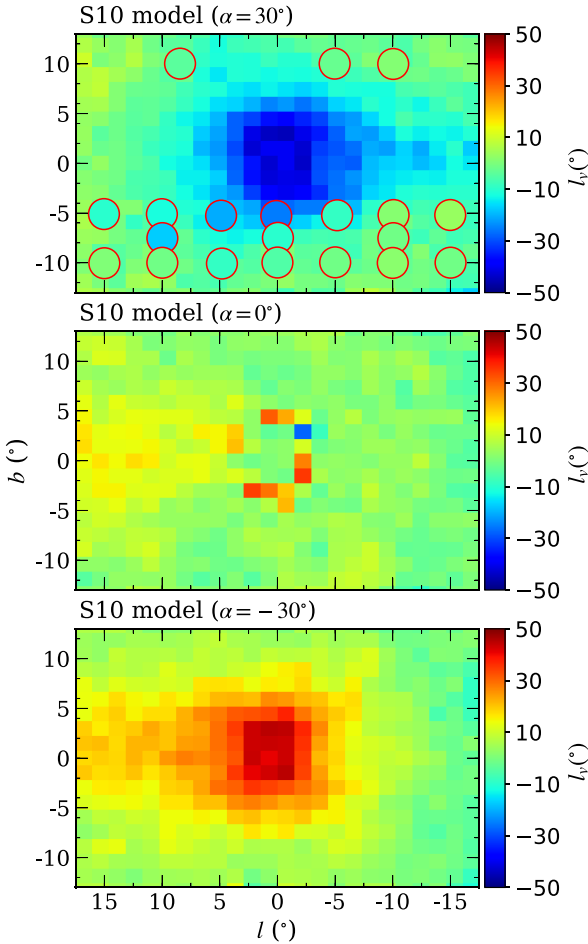


Figure 5. The l_v map of the **S10** model for 3 viewing angles: 30° (top panel), where the near end of the bar is located at positive longitudes as in the MW; 0° (middle panel) where the bar major-axis is aligned with the Sun-GC line of sight; -30° (bottom panel), where the near end of the bar is located at negative longitudes. All the particles in the simulation with $|x| < 3.5$ kpc were used for these maps. The l_v map changes when the distance distribution of the simulation is resampled to match the ARGOS distances distribution, as shown in the top panel. The resampled particles were selected from circular fields (red circles in Fig. 1) centred on the ARGOS fields.

3.3 Vertex deviation map

Another quantity that is useful in describing the velocity ellipsoid is the vertex deviation l_v (Zhao et al. 1994), the angle which measures the tilt of the longest axis of the velocity ellipsoid in the v_r-v_l plane

$$l_v = \frac{1}{2} \arctan \left(\frac{2\sigma_{rl}^2}{|\sigma_{rr}^2 - \sigma_{ll}^2|} \right), \quad (1)$$

where σ_{rl} , σ_{rr} , and σ_{ll} are the covariance and standard deviation terms of the velocity components along the line of sight (r) and longitude (l) directions. By definition, l_v takes values between -45° and $+45^\circ$.

We map the l_v variation in the simulation for three bar angles $\alpha = 30^\circ$ in Fig. 5 (top panel), $\alpha = 0^\circ$ (middle), and $\alpha = -30^\circ$ (bottom) using all particles in the **S10** model within $|x| < 3.5$ kpc. The maps provide clear evidence that l_v is strongly dependent on the bar viewing angle α , especially in the fields close to the GC, $|b| \lesssim$

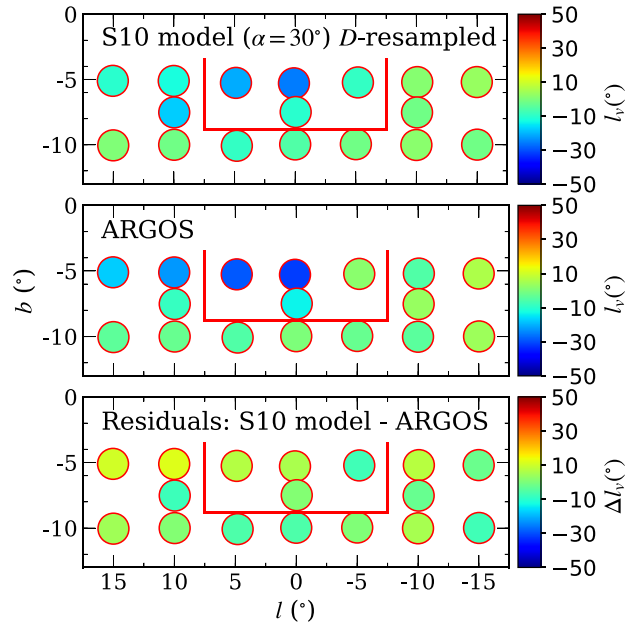


Figure 6. Top panel: Same as in top panel of Fig. 5. The l_v values were computed using only the particles within the red circles in Fig. 1. The simulation was resampled so that the heliocentric distance D distribution matches the ARGOS data sampling. Middle panel: The data l_v map is in good agreement with the resampled simulation, in particular in the 4 central fields delimited by the red lines. Bottom panel: The difference between the resampled simulation and data l_v shows no systematic trends.

7.5° . In addition, for a given α , l_v is not constant across the bulge as already suggested by the velocity trends in Fig. 2.

The vertex deviation values computed with the ARGOS–Gaia DR2 sample are in disagreement with the **S10** model predictions for $\alpha = 30^\circ$ before resampling (top panel of Fig. 5) but in good qualitative agreement after distance resampling (Fig. 6). The residuals between the distance-resampled **S10** model l_v values and the ARGOS data (bottom panel of Fig. 6) are close to 0° in most fields and show no systematic trends, proving that resampling is a fundamental step in building the **S10** model velocity ellipsoid.

In Fig. 5, we mapped the **S10** model vertex deviation for $\alpha = 0^\circ$, $\pm 30^\circ$ and showed that the bar viewing angle has a direct influence on kinematics (hence on l_v). In Fig. 7, we show the variation of l_v with α for a grid of values between -90° and $+90^\circ$, for both the resampled (green curve in Fig. 7) and the non-resampled (black curve) simulation. The black curve passes through $(\alpha, l_v) = (0^\circ, 0^\circ)$ marked with a black cross in the figure, confirming that for an axisymmetric system the vertex deviation is null across the bulge. In addition, the amplitude of the l_v variation is stronger for the non-resampled model (black curve) than for the resampled model (green curve), suggesting that the ARGOS distance sampling will slightly affect the l_v measurements. In particular, the resampling affects l_v in the low-latitude fields at $b = -5^\circ$ except for the most central field ($l, b) = (0^\circ, -5^\circ)$ which displays the strongest l_v variation with α with values between $+35^\circ$ and -35° for both the distance-resampled and non-resampled model. Slightly smaller l_v variations of $\pm 25^\circ$ can be seen in the three adjacent fields $(l, b) = \{(5^\circ, -5^\circ), (-5^\circ, -5^\circ), (0^\circ, -7.5^\circ)\}$ (delimited by the red box in Fig. 6) but they sharply decrease beyond that (Fig. 7). This is confirmed by Fig. 4 where the **S10** model velocity ellipsoids in three fields c $(0^\circ, -10^\circ)$, d $(-10^\circ, -5^\circ)$ and

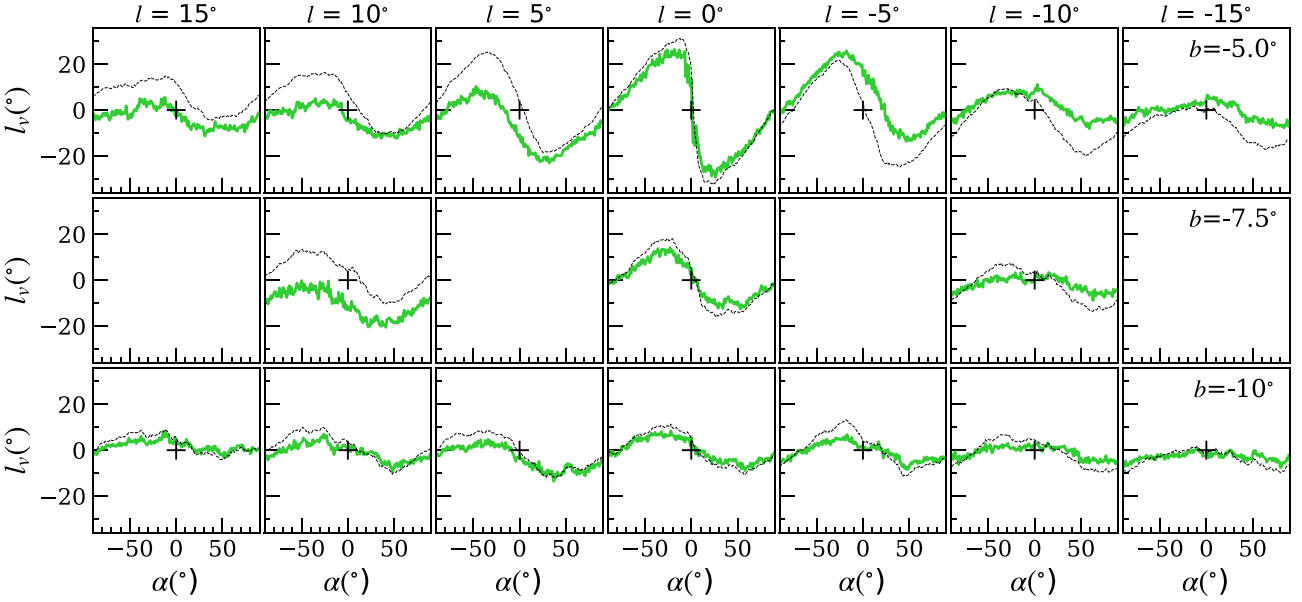


Figure 7. Vertex deviation of the resampled (green line) and non-resampled (black dotted line) model as a function of bar viewing angle, α , for 180 values between -90° and $+90^\circ$. For $\alpha = 0^\circ$, the vertex deviation is $l_v = 0^\circ$ (see black cross), therefore an axisymmetric density distribution would not generate a tilted velocity ellipsoid, as it can be seen also in the middle panel of Fig. 5. In the fields close to the GC the vertex deviation variation at $\alpha = 0^\circ$ is very steep, causing the circular artefact at $|l|, |b| < 5^\circ$.

e ($10^\circ, -5^\circ$) almost overlap for $\alpha = 30^\circ$ and $\alpha = -30^\circ$ and l_v is almost identical, a strong indication that beyond the 4 central fields, the kinematics (and l_v) is not sensitive to the bar viewing angle.

Our measurements along the minor axis are consistent with the results from Soto et al. (2012) who obtained $l_v \sim -43^\circ/40^\circ$ at $(1^\circ, -4^\circ)$ for all stars/RGBs and -17° at $(0^\circ, -6^\circ)$ for all stars. We have obtained remarkably similar results, $l_v = -40^\circ$ at $(0^\circ, -5^\circ)$ and $l_v = -19^\circ$ at $(0^\circ, -7.5^\circ)$. Both studies agree that the l_v values decrease at increasing latitudes and longitudes, away from the Galactic Centre.

In the next section, we provide a more quantitative comparison between the data and the simulation based on the velocity vectors of the individual stars.

4 RETRIEVING α FROM KINEMATICS

We aim to constrain the angle between the MW bar major-axis and the Sun-GC line α , a fundamental property of the MW bar morphology from stellar kinematics.

4.1 Kinematic modelling

We determine the most probable bar angle from kinematic observations via a maximum likelihood method. The probability density in velocity space of a bulge RC star defined by its three velocity components $V_i = \{v_l, v_b, v_r\}_i$ to belong to a model $M(\mu, \Sigma'; \alpha)$, fitted on the S10 model velocity distribution after distance resampling, is given by the Gaussian probability density function

$$p(V_i|\alpha) = \frac{1}{(2\pi)^{n/2} |\Sigma'|^{1/2}} \exp\left(-\frac{1}{2}(V_i - \mu)^T \Sigma'^{-1} (V_i - \mu)\right) \quad (2)$$

where $n = 3$ is the size of the data vector V_i , μ is the centroid of the velocity ellipsoid, and Σ' the total covariance matrix $\Sigma' = \Sigma + \Sigma_D$

where Σ is the 3×3 covariance matrix of the velocity ellipsoid

$$\Sigma = \begin{bmatrix} \sigma_{ll}^2 & \sigma_{lr}^2 & \sigma_{lb}^2 \\ \sigma_{rl}^2 & \sigma_{rr}^2 & \sigma_{rb}^2 \\ \sigma_{bl}^2 & \sigma_{br}^2 & \sigma_{bb}^2 \end{bmatrix}.$$

The diagonal terms are the velocity dispersions along the three directions $\sigma_{ll}, \sigma_{rr}, \sigma_{bb}$ and the cross terms $\sigma_{lr}^2, \sigma_{br}^2, \sigma_{lb}^2$ determine the orientation of the velocity ellipsoid. Σ_D is a diagonal matrix which contains the data uncertainties along the three velocity components, $\sigma_{v_l}^2, \sigma_{v_r}^2, \sigma_{v_b}^2$, computed using Monte Carlo resampling, as explained in Section 3.1. Both the centroid μ and the covariance matrix Σ are computed on the S10 model and are α -dependent. Throughout this work, we have abbreviated $\mu(\alpha)$ and $\Sigma(\alpha)$ with μ and Σ .

For each pointing, the probability density of the observed sample of velocities V under the model $M(\mu, \Sigma; \alpha)$ for the bar viewing angle α , is given by

$$P(V|\alpha) = \prod_{i=1}^N p(V_i|\alpha).$$

In practice, we aim to find α , for which the quantity

$$-\ln(P) = -\sum_{i=1}^N \ln p(V_i|\alpha) \quad (3)$$

is a minimum, where the sum is carried out for the total number of stars N , in each pointing. The viewing angle α_{\min} , which minimizes equation (3), is then the Maximum Likelihood (ML) estimate. The 1σ error on α_{\min} is defined by the interval $\Delta \ln(L) = 0.5$, above the minimum of the log-likelihood curve.²

²See Bevington & Robinson (2003).

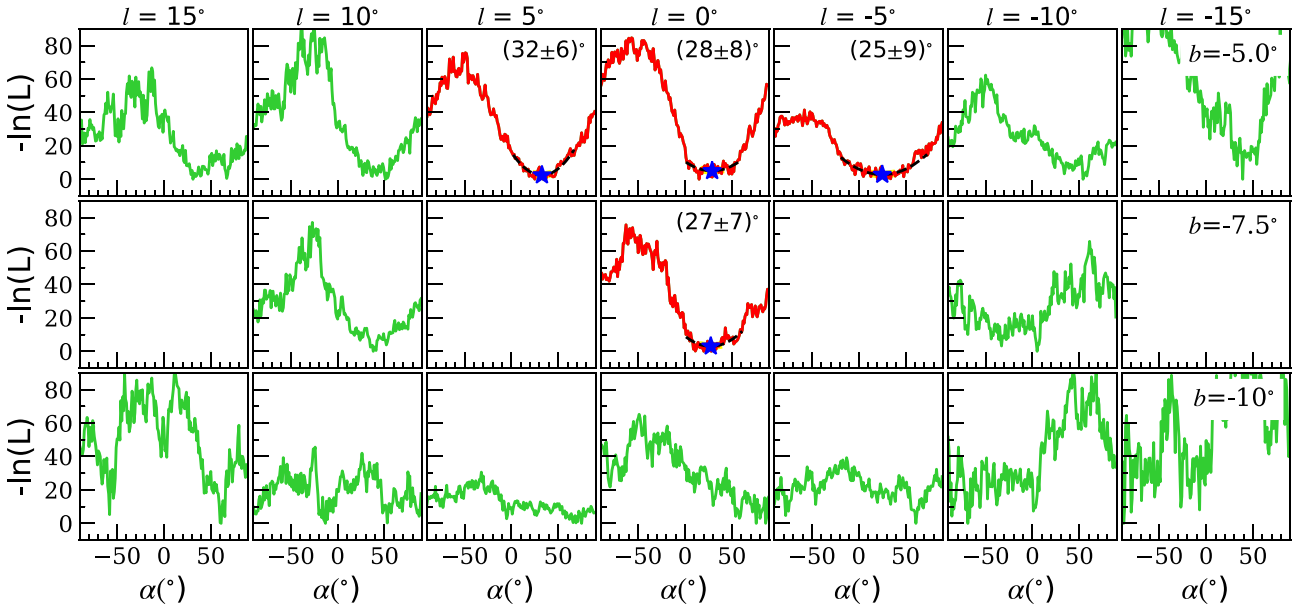


Figure 8. The log-likelihood of the data computed using the model fitted on the resampled S10 model. The blue star is the best-fitting angle in each field of view. We provide the α values for the 4 fields marked in red, and the uncertainties.

4.2 Results

We have applied the fitting method to the individual fields and we show the log-likelihood variation with α in Fig. 8. The log-likelihood was evaluated for 180 values of α using the distance-resampled S10 model (the vertex deviation of this model for each angle is given in Fig. 7 and is discussed in Section 3.3) and it reaches a minimum for different values of α in each field. In the figure, we placed the minimum log-likelihood at 0 in each pointing.

ARGOS is a survey at intermediate latitudes and it can only sample the outer edges of the bulge stellar density distribution. The fields $(l, b) = \{(5^\circ, -5^\circ), (-5^\circ, -5^\circ), (0^\circ, -7.5^\circ)\}$ are the closest to the bulge centre and contain a large proportion of bulge stars. Here, the stellar kinematics is most affected by the bar morphology as we have shown in Fig. 7: the 4 central fields exhibit large l_v variations with α and have clear minima while the outer fields have much smaller variations especially after resampling (green curve). For this reason (see also Section 3.3), to determine the best-fitting viewing angle α_{\min} we sum the log-likelihood curves only in the 4 central fields marked in red in Fig. 8. The result is shown in the left-hand panel of Fig. 9.

To determine α_{\min} , a parabola was fitted over a $\Delta \ln(L) = 40.5$ (9σ) interval (black dashed line around the minimum). The final value is $\alpha_{\min} = (29 \pm 3)^\circ$. This value is an independent measure of the MW bar viewing angle from the kinematics of ~ 7000 ARGOS–Gaia DR2 RC stars, and is consistent with previous studies of bar morphology using star counts (Stanek et al. 1997; Cao et al. 2013; Wegg & Gerhard 2013; Simion et al. 2017 – see their fig. 17 for a comparison between different works)

4.3 Validation tests

4.3.1 Mock sample

We test whether we are able to recover the correct bar angle of a mock sample of particles drawn from the S10 simulation with the

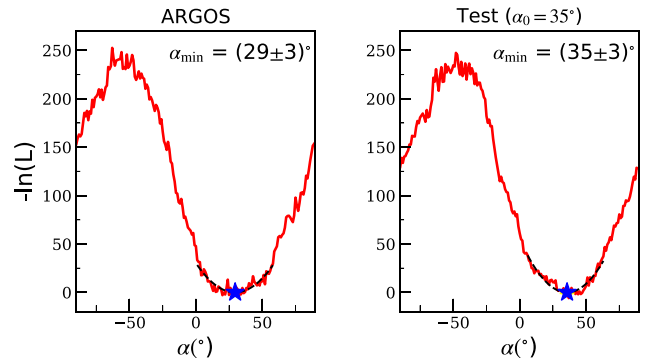


Figure 9. Left-hand panel: Final result obtained from the sum of the log-likelihood curves in the 4 fields marked in red in Fig. 8. The minimum is obtained at $\alpha_{\min} = (29 \pm 3)^\circ$, where the uncertainty was computed over a 9σ interval. Right-hand panel: We performed a test on a mock sample with $\alpha_0 = 35^\circ$ and the same distance distribution as the data. We have done the test using different angles for the mock sample, and each time we successfully recover the true angle, α_0 .

bar major-axis at a given angle α_0 with the Sun-GC line, replicating the same fitting procedure applied to the data.

The mock sample distances include realistic heliocentric distance errors, modelled assuming a Gaussian error distribution with a standard deviation of $\sigma_D \approx \delta_{M_K} \times 0.2 \times D \times \ln(10)$. From the perturbed sample, in each field, we draw the same number of particles as in our data sample, according to the probability distribution of the ARGOS distances in each field. Thus, the distances of the mock stars are not matching the initial positions in the simulation, which in turn affects the velocity distribution. In addition, we have assigned a constant velocity error to the mock particles in each field, corresponding to the median uncertainty on each of the 3 velocity components in the data. To summarize, the mock sample has realistic velocity and distance errors, the same number of particles as the data, and the same distance distribution.

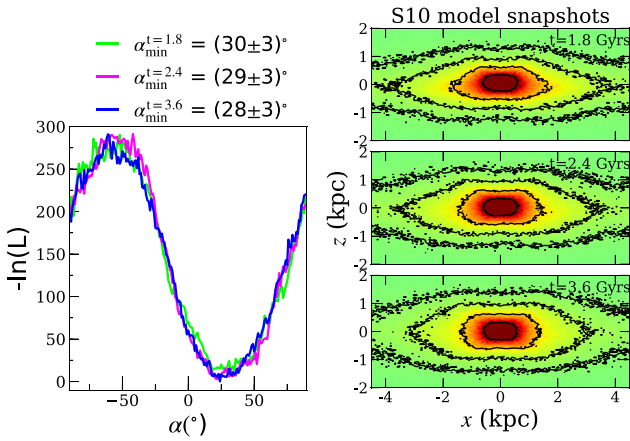


Figure 10. *Left-hand panel:* Same as in the left-hand panel of Fig. 9 but here the model was constructed using three early snapshots of the S10 model, at 1.8, 2.4, and 3.6 Gyrs. Although the models have different density distributions, the angle α_0 could be recovered successfully. *Right-hand panel:* The density distribution of the S10 model projected on the x - z plane at 1.8 (top), 2.4 (middle), and 3.6 Gyrs (bottom).

We compute the log-likelihood values for the mock sample on a grid of 180 α values between -90° and $+90^\circ$, following the same kinematic modelling procedure described in Section 4.1. The sum of the $\ln(L)$ curves in the 4 central fields is shown in Fig. 9, right-hand panel, where $\alpha_0 = 35^\circ$ is the bar angle set for the mock catalogue and $\alpha_{\min} = 35 \pm 3^\circ$ is the retrieved bar viewing angle. We repeated this test for numerous random samples and different α_0 and, despite the small number of mock particles of around $N \sim 400$ per field of view (matching the RC sample), the mock catalogue’s viewing angle α_0 can be recovered. The best-fitting value was found fitting a parabola over an α interval in which $\ln(L)$ varies by 9σ , or $\Delta\ln(L) = 40.5$ (dotted curve). We have also tested different intervals to check that a 9σ interval is adequate: an interval of 8–10 σ would produce an identical result and intervals within 5–12 σ would produce a variation smaller than $\pm 3^\circ$, however, the exact input value could be obtained for a 8–10 σ interval. This led us to adopt a 9σ interval for the data (left-hand panel of the figure).

4.3.2 S10 model snapshots

The S10 model used in this work is a specific instance of a simulated galaxy and while it has been successful at matching observations in the bulge region, it is likely not a perfect match to the MW due to its simple nature. To check whether small differences in the model density distribution will affect our determination of the bar angle α from the *Gaia*–ARGOS stellar kinematics, we test our kinematic modelling using three snapshots of the S10 model at early times, 1.8, 2.4, and 3.6 Gyrs. Their density distribution projected on to the x - z plane is shown in Fig. 10, right-hand panel. At 1.8 and 2.4 Gyrs the bulge density distribution is not completely symmetric with respect to the Galactic Plane, but at later times (see $t = 3.6$ Gyrs), as the buckling instability gradually saturates, it becomes increasingly symmetric. MW observations suggest that our bulge is relatively symmetric with respect to the plane therefore later snapshots may provide a better description of the bulge. We repeat the kinematic modelling procedure using the three earlier snapshots and find that the best estimates of α (Fig. 10, left-hand panel) are consistent with the value $\alpha_{\min} = 29^\circ$ we found using the canonical S10 model at $t = 4.8$ Gyrs (Fig. 9, left-hand panel). The test suggests that the result

of our fitting method will not be affected by small changes in the density distribution of the model, likely because of the large distance and v_l errors that were implemented in the model to mimic the data.

4.3.3 Distance systematic offsets

A distance offset could be introduced if, for example, the intrinsic magnitude M_K of the RC was under/overestimated. The presence of a younger RC population would also introduce a systematic offset: the RC of a 5 Gyrs population is -0.1 mag brighter than that of a 10 Gyrs population, the bulge age commonly assumed. Simion et al. (2017) estimated that such a population would be predominantly located within $|b| < 4^\circ$, therefore it should not have a large contribution to the ARGOS fields.

The ARGOS collaboration assume $M_K = -1.61$ mag for the RC. As a test, we have updated the ARGOS distances assuming two other values, $M_K = -1.51$ and $M_K = -1.81$. We have then applied the fitting method described in Section 4.1 to the updated data sets. The best-fitting viewing angles we retrieved are $\alpha = (31 \pm 3)^\circ$ and $\alpha = (24 \pm 3)^\circ$, respectively. We note that the typical uncertainty expected for the RC stars $\sigma_{M_K} \sim 0.22$ is taken into account in the fitting procedure.

We are aware that the parallaxes reported by *Gaia* DR2 have a systematic offset of ~ -0.03 mas (Lindgren et al. 2018) which can potentially translate into proper motion systematic offsets, via the cross-terms. Such offsets could affect our computations of v_l and v_b , and finally of l_v . Performing Monte Carlo resampling we computed the effect of the parallax offset on the velocities and we found that they change by less than 5 km s^{-1} ; in fact, the majority of v_l (65 per cent) and v_b (80 per cent) have only changed by 1 km s^{-1} . The effect on l_v is smaller than 0.1° .

4.3.4 RGB contamination

We have also tested how a 30 per cent contamination rate from the RGB stars would affect our results. In each field of view, we draw new M_K values for 30 per cent of the targets between -3 and $+0.5$ mag from an exponential distribution which is commonly used to model the RGB, using the parameters computed by Simion et al. (2017). We ran the fitting procedure on the new data set where 70 per cent of the sample remained unaltered. While the best-fitting α values in the individual fields vary by $\pm 2^\circ$ compared to the values reported in Fig. 7, the final result remains $\alpha = (29 \pm 3)^\circ$.

5 VERTEX DEVIATION AS A FUNCTION OF METALLICITY

In this section, we investigate the metallicity-kinematics correlation in all ARGOS fields.

We split the sample in each pointing into three metallicity populations, following the definitions in Ness et al. (2013a): the high metallicity component A, intermediate metallicity component B, and the low metallicity component C. The metal poor components D and E have very few numbers of stars (see their weights in table 3, Ness et al. 2013a) and we classify them as component C according to the decision boundaries determined using the parameters in tables 2 and 3 in Ness et al. (2013a). As it is apparent from figs 11 and 12 in Ness et al. (2013a), the decision boundaries and the weights of each metallicity component vary with latitude, as is expected due to the bulge metallicity gradient (e.g. Gonzalez et al. 2013). In Fig. 11, we show the vertex measurements in each field as a

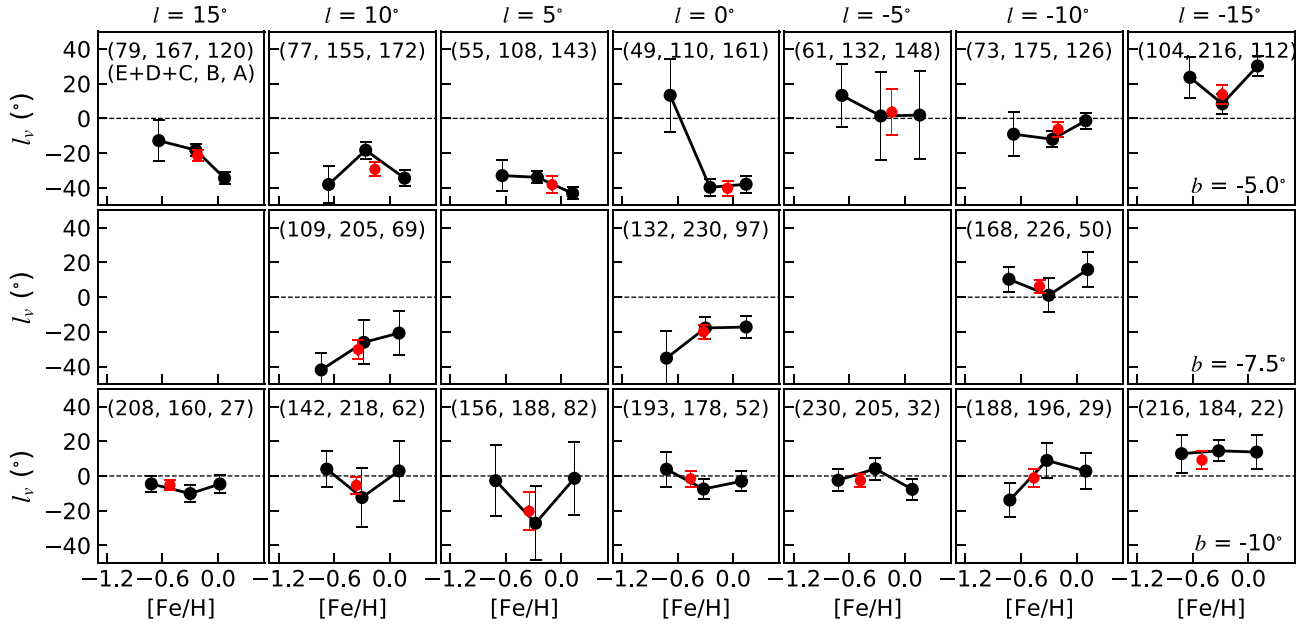


Figure 11. Vertex deviation variation with metallicity. For each pointing, the number of stars in each metallicity components is given in the upper left corner. Because of the bulge metallicity gradient with latitude, there are more metal-rich stars close to the Galactic Plane than at lower latitudes. The vertex deviation and the median metallicity for all stars in a given pointing is marked with red.

function of metallicity for all stars in the field (red) and for the 3 sub-populations (black). The l_v uncertainties shown in Fig. 11, are the standard deviation of 500 l_v evaluations on as many bootstrap resampling trials. In the inset we specify the number of stars in each component, with the metal-poor population C+E+D in the left.

The field at $(0^\circ, -5^\circ)$ is the closest to the GC and here l_v is most sensitive to changes of α (see Fig. 7). From Fig. 11, we notice that it also displays the strongest l_v trend with metallicity, in very good agreement with earlier studies and simulations in Baade’s window at $l, b \sim (1^\circ, -4^\circ)$ (Soto et al. 2007; Babusiaux 2016; Debattista et al. 2019): metal-rich stars with $[\text{Fe}/\text{H}] > -0.5$ have a much higher vertex deviation ($l_v \sim -40^\circ$) than metal poor stars $[\text{Fe}/\text{H}] < -0.5$ ($l_v \sim 15^\circ$).

The fields at $b = -10^\circ$ are consistent with $l_v \sim 0^\circ$ at all metallicities as expected (see the last row of Fig. 7) while for the remaining fields we do not observe obvious trends. The stars at $l > 0^\circ$ (left-hand panels in Fig. 11) will likely belong to the near end of the bar, while the stars at $l < 0^\circ$ (right-hand panels in Fig. 11), will either be located in the far end of the bar or in the foreground disc population, due to the ARGOS sampling which preferentially targets closer stars. The vertex deviation of an axisymmetric system such as the disc, should be $l_v \sim 0^\circ$, close to the values we compute in several metallicity bins at $l < 0^\circ$.

6 CONCLUSION

We have compiled a sample of ~ 7000 bulge RC stars with 6D phase-space information and metallicity from ARGOS and *Gaia* DR2. The sample is large enough to allow for a comprehensive study of the bulge kinematics at intermediate latitudes:

- (i) We mapped the ARGOS–*Gaia* DR2 velocity distributions in Fig. 2 and bulge velocity ellipsoids in Fig. 3;
- (ii) For a specific instance of a simulated galaxy (the S10 model) we have built maps of the bulge vertex deviation for three bar viewing

angles $\alpha = +30^\circ, 0^\circ, -30^\circ$ (Fig. 5). The significant differences between the three maps indicate that the bulge morphology has a direct impact on the bulge kinematics;

(iii) We have used the S10 model to show the l_v variation with α and found that $l_v \sim 0^\circ$ in all fields when either of the bulge axes is aligned with the Sun-GC line of sight (Fig. 7), as expected for axisymmetric systems;

(iv) We evaluated the probability of our data set on a star-by-star basis to belong to a kinematic model based on the resampled S10 model via a maximum-likelihood method (Fig. 8). The most likely bar angle we retrieved is $\alpha_{\text{min}} = (29 \pm 3)^\circ$, with an additional uncertainty due to comparison with one specific model.

We have thus obtained an independent measurement of the MW bar viewing angle from kinematic data alone. In this work we have chosen the S10 model for kinematic modelling (Section 4) because of its simplicity and because it is able to reproduce a large number of the MW bulge morphological and kinematical properties (Section 1). Systematic biases resulting from model mismatches with the MW (e.g. density distribution, bar pattern speed) are difficult to estimate. In Section 4.3.2, we have shown that small changes in the model density distribution provide consistent best-fitting α values. In the future it will be useful to quantify possible biases using different models, in particular more complex bar models should be used for modelling the kinematics at lower latitudes. The quality of data may also be responsible for fluctuations in the best-fitting α measurement. For instance, in Section 4.3 we have found that the RGB contamination does not significantly affect our result but the intrinsic magnitude assumed for the RC can alter the result in a major way: an offset of ± 0.2 mag (± 0.1 mag) would produce an α change of $\pm 5^\circ$ ($\pm 2^\circ$).

In the four central fields centred on $(l, b) = \{(0^\circ, -5^\circ), (5^\circ, -5^\circ), (-5^\circ, 5^\circ), (0^\circ, -7.5^\circ)\}$, the tilt of the S10 model velocity ellipsoids l_v is very sensitive to the bar viewing angle α and it takes values between $l_v \sim +45^\circ$ and $l_v \sim -45^\circ$ (Fig. 7). These four fields

were therefore chosen to derive α_{\min} as the adjacent fields have smaller l_v - α variation and do not have as much constraining power. At $b = -10^\circ$ the log-likelihood curves are too noisy and were not considered. Finally, distance resampling was a key ingredient of our kinematic modelling. In the top panels of Figs 5 and 6, we show the l_v map in the S10 model before and after distance resampling, respectively, and found that only the latter can match the ARGOS-*Gaia* DR2 data (Fig. 6). Using the S10 model we have also showed that incompleteness could affect the constraining power of the data: the amplitude of the l_v variation with α is larger for a complete sample, as evidenced by the non-resampled S10 model (black curve, Fig. 7) compared to a resampled model (green). Future studies using more complete data should be able to determine α also in the outer bulge fields.

The variation of the vertex deviation with metallicity is consistent with previous studies in Baade's window, with metal-rich stars having a higher vertex deviation than metal-poor stars. With a more complete sample it will be possible to draw firmer conclusions about the vertex deviation variation with metallicity in the remaining fields; however, at low latitudes where the bar does not affect the kinematics, the values are all consistent with $l_v \sim 0^\circ$ as expected for an axi-symmetric system. The Blanco DECam Bulge Survey (Johnson et al. 2020) is a photometric survey that can provide metallicities for millions of bulge stars for which *Gaia* proper motions are readily available. But before we can reproduce the results in Fig. 5 with an increased number of stars, more radial velocities at bulge distances are needed.

ACKNOWLEDGEMENTS

ITS thanks the referee for the constructive comments that helped improve the manuscript and is grateful for the valuable discussions with V. Belokurov, J. Fernandez-Trincado, A. Robin, Z. Yuan, G. Iorio, and V. Debattista. ITS acknowledges support from the PIFI Grant n. 2018PM0050 and LAMOST. The research presented here is partially supported by the National Key R&D Program of China under grant no. 2018YFA0404501; by the National Natural Science Foundation of China under grant nos. 12025302, 11773052, 11761131016; by the 111 Project of the Ministry of Education under grant no. B20019. JS acknowledges support from a Newton Advanced Fellowship awarded by the Royal Society and the Newton Fund. SK is partially supported by NSF grants AST-1813881, AST-1909584 and Heising-Simons Foundation grant 2018-1030.

DATA AVAILABILITY

The 2MASS-*Gaia* DR2 data underlying this article are available in the gaiadr2.tmass_best_neighbour folder, at <https://gea.esac.esa.int/archive/>. The ARGOS data were provided by the ARGOS collaboration. Data can be shared on request to the corresponding author with permission of the ARGOS collaboration.

REFERENCES

Alves D. R., 2000, *ApJ*, 539, 732
 Athanassoula E., Rodionov S. A., Peschken N., Lambert J. C., 2016, *ApJ*, 821, 90
 Athanassoula E., Rodionov S. A., Prantzos N., 2017, *MNRAS*, 467, L46
 Babusiaux C., 2016, *PASA*, 33, e026
 Babusiaux C. et al., 2010, *A&A*, 519, A77
 Bender R., Burstein D., Faber S. M., 1992, *ApJ*, 399, 462
 Bevington P. R., Robinson D. K., 2003, *Data Reduction and Error Analysis for the Physical Sciences*, 3rd edn. McGraw-Hill, New York, NY

Bovy J., Hogg D. W., Roweis S. T., 2011, *Ann. Appl. Stat.*, 5, 1657
 Cao L., Mao S., Nataf D., Rattenbury N. J., Gould A., 2013, *MNRAS*, 434, 595
 Clarke J. P., Wegg C., Gerhard O., Smith L. C., Lucas P. W., Wylie S. M., 2019, *MNRAS*, 489, 3519
 Clarkson W. et al., 2008, *ApJ*, 684, 1110
 Combes F., Debbasch F., Friedli D., Pfenniger D., 1990, *A&A*, 233, 82
 de Zeeuw T., 1992, in DeJonghe H., Habing H. J., eds, *Proc. IAU Symp.* 153, Galactic Bulges. Kluwer Academic Publishers, Dordrecht, p. 191
 Debattista V. P., Carollo C. M., Mayer L., Moore B., 2005, *ApJ*, 628, 678
 Debattista V. P., Ness M., Earp S. W. F., Cole D. R., 2015, *ApJ*, 812, L16
 Debattista V. P., Ness M., Gonzalez O. A., Freeman K., Zoccali M., Minniti D., 2017, *MNRAS*, 469, 1587
 Debattista V. P., Gonzalez O. A., Sanderson R. E., El-Badry K., Garrison-Kimmel S., Wetzel A., Faucher-Giguère C.-A., Hopkins P. F., 2019, *MNRAS*, 485, 5073
 Di Matteo P., Fragkoudi F., Khoperskov S., Ciambur B., Haywood M., Combes F., Gómez A., 2019, *A&A*, 628, A11
 Eggen O. J., Lynden-Bell D., Sandage A. R., 1962, *ApJ*, 136, 748
 Fragkoudi F., Di Matteo P., Haywood M., Gómez A., Combes F., Katz D., Semelin B., 2017, *A&A*, 606, A47
 Freeman K. et al., 2013, *MNRAS*, 428, 3660
 Gaia Collaboration, 2016, *A&A*, 595, A1
 Gillessen S. et al., 2017, *ApJ*, 837, 30
 Girardi L., 2016, *ARA&A*, 54, 95
 Gonzalez O. A., Rejkuba M., Zoccali M., Valent E., Minniti D., Tobar R., 2013, *A&A*, 552, A110
 Häfner R., Evans N. W., Dehnen W., Binney J., 2000, *MNRAS*, 314, 433
 Hawkins K., Leistedt B., Bovy J., Hogg D. W., 2017, *MNRAS*, 471, 722
 Hill V. et al., 2011, *A&A*, 534, A80
 Howard C. D. et al., 2009, *ApJ*, 702, L153
 Johnson C. I. et al., 2020, *MNRAS*, 499, 2357
 Kormendy J., Kennicutt, Robert C. J., 2004, *ARA&A*, 42, 603
 Kozłowski S., Woźniak P. R., Mao S., Smith M. C., Sumi T., Vestrand W. T., Wyrzykowski Ł., 2006, *MNRAS*, 370, 435
 Kuijken K., Rich R. M., 2002, *AJ*, 124, 2054
 Kunder A. et al., 2012, *AJ*, 143, 57
 Li Z.-Y., Shen J., 2012, *ApJ*, 757, L7
 Lindegren L. et al., 2018, *A&A*, 616, A2
 Martinez-Valpuesta I., Shlosman I., Heller C., 2006, *ApJ*, 637, 214
 McWilliam A., Zoccali M., 2010, *ApJ*, 724, 1491
 Minniti D. et al., 2010, *New A*, 15, 433
 Molloy M., Smith M. C., Evans N. W., Shen J., 2015a, *ApJ*, 812, 146
 Molloy M., Smith M. C., Shen J., Evans N. W., 2015b, *ApJ*, 804, 80
 Nataf D. M., Udalski A., Gould A., Fouqué P., Stanek K. Z., 2010, *ApJ*, 721, L28
 Nataf D. M., Cassisi S., Athanassoula E., 2014, *MNRAS*, 442, 2075
 Nataf D. M. et al., 2015, *MNRAS*, 447, 1535
 Ness M., Lang D., 2016, *AJ*, 152, 14
 Ness M. et al., 2012, *ApJ*, 756, 22
 Ness M. et al., 2013a, *MNRAS*, 430, 836
 Ness M. et al., 2013b, *MNRAS*, 432, 2092
 Ness M. et al., 2016, *ApJ*, 819, 2
 Portail M., Gerhard O., Wegg C., Ness M., 2017, *MNRAS*, 465, 1621
 Qin Y., Shen J., Li Z.-Y., Mao S., Smith M. C., Rich R. M., Kunder A., Liu C., 2015, *ApJ*, 808, 75
 Quillen A. C., Minchev I., Sharma S., Qin Y.-J., Di Matteo P., 2014, *MNRAS*, 437, 1284
 Raha N., Sellwood J. A., James R. A., Kahn F. D., 1991, *Nature*, 352, 411
 Rattenbury N. J., Mao S., Debattista V. P., Sumi T., Gerhard O., de Lorenzi F., 2007, *MNRAS*, 378, 1165
 Rich R. M., Reitzel D. B., Howard C. D., Zhao H., 2007, *ApJ*, 658, L29
 Robin A. C., Marshall D. J., Schultheis M., Reylé C., 2012, *A&A*, 538, A106
 Saha K., Gerhard O., 2012, in Buta R., Pfenniger D., eds, *Proceeding of the XXVIII IAU General Assembly, Special Session 3: Galaxy Evolution through Secular Processes*, preprint ([arXiv:1212.4579](https://arxiv.org/abs/1212.4579))
 Saito R. K., Zoccali M., McWilliam A., Minniti D., Gonzalez O. A., Hill V., 2011, *AJ*, 142, 76

- Sanders J. L., Smith L., Evans N. W., 2019a, *MNRAS*, 488, 4552
- Sanders J. L., Smith L., Evans N. W., Lucas P., 2019b, *MNRAS*, 487, 5188
- Schönrich R., Binney J., Dehnen W., 2010, *MNRAS*, 403, 1829
- Sellwood J. A., Gerhard O., 2020, *MNRAS*, 495, 3175
- Shen J., 2014, in Feltzing S., Zhao G., Walton N. A., Whitelock P., eds, Proc. IAU Symp. 298, Setting the Scene for Gaia and LAMOST. Kluwer, Dordrecht, p. 201
- Shen J., Li Z.-Y., 2016, in Laurikainen E., Peletier R., Gadotti D., eds, Astrophysics and Space Science Library, Vol. 418, Theoretical Models of the Galactic Bulge. Springer-Verlag, Berlin, p. 233
- Shen J., Rich R. M., Kormendy J., Howard C. D., De Propris R., Kunder A., 2010, *ApJ*, 720, L72 (S10)
- Simion I. T., Belokurov V., Irwin M., Koposov S. E., Gonzalez-Fernandez C., Robin A. C., Shen J., Li Z. Y., 2017, *MNRAS*, 471, 4323
- Skrutskie M. F. et al., 2006, *AJ*, 131, 1163
- Smith L. C. et al., 2018, *MNRAS*, 474, 1826
- Soto M., Rich R. M., Kuijken K., 2007, *ApJ*, 665, L31
- Soto M., Kuijken K., Rich R. M., 2012, *A&A*, 540, A48
- Soto M., Zeballos H., Kuijken K., Rich R. M., Kunder A., Astraatmadja T., 2014, *A&A*, 562, A41
- Spaenhauer A., Jones B. F., Whitford A. E., 1992, *AJ*, 103, 297
- Stanek K. Z., Mateo M., Udalski A., Szymanski M., Kaluzny J., Kubiak M., 1994, *ApJ*, 429, L73
- Stanek K. Z., Udalski A., Szymański M., Kałużny J., Kubiak Z. M., Mateo M., Krzemiński W., 1997, *ApJ*, 477, 163
- Sumi T. et al., 2004, *MNRAS*, 348, 1439
- The GRAVITY Collaboration, 2019, *A&A*, 625, L10
- Vanderplas J., Connolly A., Ivezić Ž., Gray A., 2012, Conference on Intelligent Data Understanding (CIDU), p. 47
- Vásquez S. et al., 2013, *A&A*, 555, A91
- Wegg C., Gerhard O., 2013, *MNRAS*, 435, 1874
- Wegg C., Gerhard O., Portail M., 2015, *MNRAS*, 450, 4050
- Wegg C., Rojas-Arriagada A., Schultheis M., Gerhard O., 2019, *A&A*, 632, A121
- Zasowski G., Ness M. K., García Pérez A. E., Martínez-Valpuesta I., Johnson J. A., Majewski S. R., 2016, *ApJ*, 832, 132
- Zhao H., Spergel D. N., Rich R. M., 1994, *AJ*, 108, 2154

This paper has been typeset from a \LaTeX file prepared by the author.